ON THE MERGING CLUSTER ABELL 578 AND ITS CENTRAL RADIO GALAXY 4C +67.13[1]

K. Hagino[1,2], Ł. Stawarz[1,3], A. Siemiginowska[4], C.C. Cheung[5], D. Kozieł-Wierzbowska[3], A. Szostek[3], G. Madejski[6], D.E. Harris[4], A. Simionescu[1], and T. Takahashi[1,2]

[1]Institute of Space and Astronautical Science JAXA, 3-1-1 Yoshinodai, Chuo-ku, Sagamihara, Kanagawa 252-5210, Japan
[2]Department of Physics, University of Tokyo, 7-3-1 Hongo, Bunkyo, Tokyo 113-0033, Japan
[3]Astronomical Observatory, Jagiellonian University, ul. Orla 171, 30-244 Kraków, Poland
[4]Harvard Smithsonian Center for Astrophysics, 60 Garden St, Cambridge, MA 02138, USA
[5]Space Science Division, Naval Research Laboratory, Washington, DC 20375, USA
[6]W. W. Hansen Experimental Physics Laboratory, Kavli Institute for Particle Astrophysics and Cosmology, Department of Physics and SLAC National Accelerator Laboratory, Stanford University, Stanford, CA 94305, USA
Draft version March 26, 2015

ABSTRACT

Here we analyze radio, optical, and X-ray data for a peculiar cluster Abell 578. This cluster is not fully relaxed and consists of two merging sub-systems. The brightest cluster galaxy, CGPG 0719.8+6704, is a pair of interacting ellipticals with projected separation ~ 10 kpc, the brighter of which hosts the radio source 4C +67.13. The Fanaroff-Riley type-II radio morphology of 4C +67.13 is unusual for central radio galaxies in local Abell clusters. Our new optical spectroscopy revealed that both nuclei of the CGPG 0719.8+6704 pair are active, albeit at low accretion rates corresponding to the Eddington ratio $\sim 10^{-4}$ (for the estimated black hole masses of $\sim 3 \times 10^8 \, M_\odot$ and $\sim 10^9 \, M_\odot$). The gathered X-ray (*Chandra*) data allowed us to confirm and to quantify robustly the previously noted elongation of the gaseous atmosphere in the dominant sub-cluster, as well as a large spatial offset (~ 60 kpc projected) between the position of the brightest cluster galaxy and the cluster center inferred from the modeling of the X-ray surface brightness distribution. Detailed analysis of the brightness profiles and temperature revealed also that the cluster gas in the vicinity of 4C +67.13 is compressed (by a factor of about ~ 1.4) and heated (from $\simeq 2.0$ keV up to 2.7 keV), consistent with the presence of a weak shock (Mach number ~ 1.3) driven by the expanding jet cocoon. This would then require the jet kinetic power of the order of $\sim 10^{45}$ erg s^{-1}, implying either a very high efficiency of the jet production for the current accretion rate, or a highly modulated jet/accretion activity in the system.

Subject headings: galaxies: active — galaxies: individual (4C +67.13) — galaxies: clusters: individual (Abell 578) — intergalactic medium — galaxies: jets — X-rays: galaxies: clusters

1. INTRODUCTION

Relativistic jets produced in active galactic nuclei (AGN) are thought to play a major role in shaping the co-evolution of supermassive black holes (SMBHs) and galaxies via widely discussed, though still hardly understood, feedback processes (see the topical reviews by Fabian 2012; Kormendy & Ho 2013). The most direct manifestation of the impact the jets make on their environment is the presence of cavities inflated in the intergalactic/intracluster medium at the position of jet cocoons (or 'radio lobes'), which are often accompanied by shock waves driven in the surrounding hot, X-ray emitting gas (see, e.g., McNamara & Nulsen 2012, and references therein).

The more luminous the jets are, the more dramatic their influence is on the ambient medium. It has been argued in particular, that high-power jets are necessary to explain the observed properties of the central parts of rich clusters as due to mechanical gas heating by expanding lobes (see, e.g., Voit & Donahue 2005; Mathews & Guo 2011). These high-powers are equivalent

to those in radio-loud quasars and their parent population of Fanaroff-Riley type-II radio galaxies (hereafter FR IIs). Yet, most of the jetted AGN found in the centers of nearby clusters are low-power systems, with large-scale edge-dimmed FR I radio morphologies (e.g., Zirbel 1997; Wing & Blanton 2011). One notable exception from this rule is the FR II radio galaxy Cygnus A, located in the center of a rich cluster (Carilli & Barthel 1996). This source is considered to be representative of high-redshift radio galaxies since in the earlier Universe, when the bulk of the feedback process took place, powerful AGN with luminous jets are being found also in dense environments (e.g., Siemiginowska et al. 2005; Belsole et al. 2007; Antognini et al. 2012)

In order to increase the sample of FR II radio sources studied in nearby clusters, we examined the NRAO[2] Very Large Array (VLA) imaging survey of Abell clusters with richness $R \geq 0$ (Owen et al. 1992; Owen & Ledlow 1997). We found that within the redshift range $z < 0.25$ and at the northern declinations visible to the VLA, only two FR II radio galaxies are hosted by brightest cluster galaxies (BCGs) in this sample: PKS B1358−113 in Abell 1836 and 4C +67.13 in Abell 578. For these two

email: hagino@astro.isas.jaxa.jp

[2] The National Radio Astronomy Observatory is a facility of the National Science Foundation operated under cooperative agreement by Associated Universities, Inc.
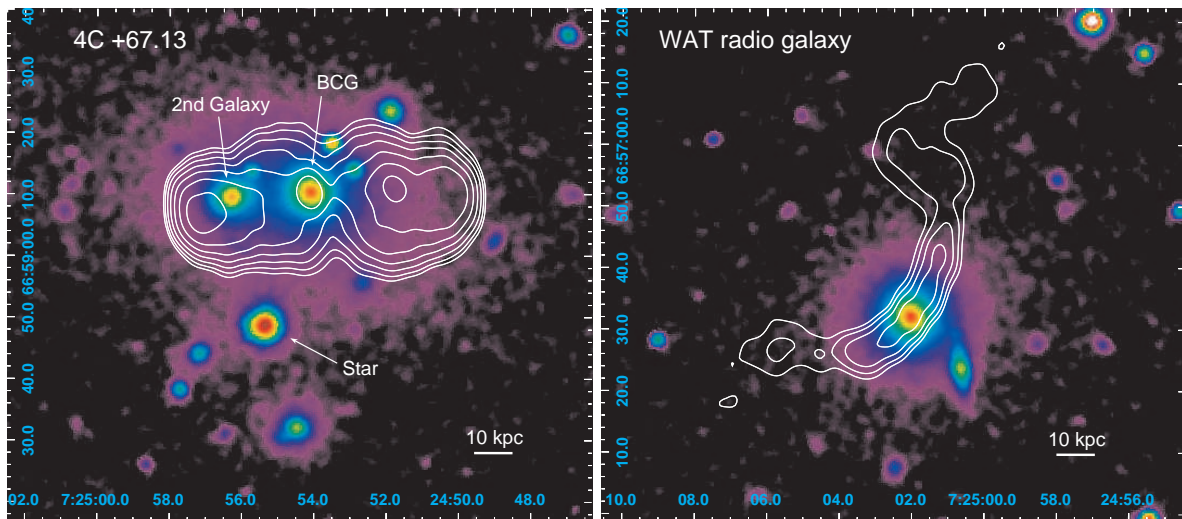
FIG. 1.— VLA 4.7 GHz contours (levels start at 0.2 mJy beam^{-1} and increase by factors of two) of the two radio galaxies found in the Abell 578 cluster superimposed on smoothed optical SDSS i-band images. The left panel shows the BCG-hosted 4C +67.13, and the right panel shows the WAT radio galaxy located in the southern part of the cluster. The fainter second galaxy adjacent to the 4C +67.13 host, which is seen through the eastern radio lobe (in projection), is the other member of the galaxy pair CGPG 0719.8+6704. A bright optical source visible to the south of 4C +67.13 is a foreground star. Throughout, coordinates are in J2000.0 equinox.

systems, we have re-analyzed archival VLA maps, acquired new optical spectra using the William Herschel Telescope (WHT), and obtained new X-ray data with Chandra and XMM-Newton. In this paper we present the analysis[3] of 4C +67.13/Abell 578, which is a peculiar example of a cluster in formation. The companion study of PKS B1358−113/Abell 1836 is presented in Stawarz et al. (2014).

Based on a detailed analysis of the velocity measurements for the cluster member galaxies, along with ROSAT PSPC data, Gomez et al. (1997) concluded that Abell 578 (cluster richness $R = 0$) is not relaxed, and consists of two interacting sub-clusters with a velocity difference of ~ 1300 km s^{-1}. The BCG is associated with the dominant cluster, and is the brighter of a pair of interconnected red spherical compacts as noted by Zwicky (1971) and catalogued by him as CGPG 0719.8+6704. The radio galaxy 4C +67.13 is hosted by the BCG and is characterized by an FR II large-scale morphology (Owen & Ledlow 1997, designated as 0719+670 therein), and hence potentially by a high jet kinetic power. At the southern end of this dominant cluster is the sub-cluster containing another radio galaxy, designated as 0720+670 by Owen & Ledlow (1997), which is of the 'wide-angle tailed' (WAT) type (see Section 2). Both radio galaxies are at rest with respect to their sub-clusters (Gomez et al. 1997).

Below, we assume a standard cosmology with $H_0 = 71$ km s^{-1} Mpc^{-1}, $\Omega_{\rm m} = 0.27$ and $\Omega_\Lambda = 0.73$, so that the redshift of the target $z = 0.0866$ (Owen et al. 1995) corresponds to the luminosity distance of $d_{\rm L} = 391$ Mpc and the conversion scale of 1.604 kpc per arcsecond.

2. RADIO DATA

Archival VLA data at two frequencies were analyzed to compare the 4C +67.13 radio morphology at arcsecond-

[3] The XMM-Newton data we obtained in this case was entirely contaminated by background flares and is not considered in this paper.

resolution with the newly acquired Chandra X-ray maps. We combined multi-configuration 1.5 GHz data obtained in 1991 when the VLA was in its A- (Sep 8; program AL238, 6 min. integration) and C-arrays (Jan 29; AO104, 5.5 min.), together with B-array data from 2001 May 7 (AC582, 1.5 hrs). At 4.7 GHz, we analyzed a single deep (2 hr) C-array dataset from 2001 July 20 (program AC582). We used AIPS for the standard calibration and DIFMAP (Shepherd et al. 1994) for self-calibration and imaging. The resultant map beamsizes were $3.12'' \times 2.03''$ (position angle, $PA = 43.2°$) at 1.5 GHz and $5.05'' \times 3.21''$ ($PA = 12.4°$) at 4.7 GHz.

The VLA contours of 4C +67.13 superimposed on the Sloan Digital Sky Survey (SDSS; York et al. 2000) optical image are shown in Figure 1 (left panel). Note that despite its edge-brightened FR II radio morphology, the studied radio galaxy does not obviously show compact high surface brightness hotspots at the edges of the radio lobes. With a total linear size of $47'' \simeq 75$ kpc and axial ratio $\simeq 2$, which is typical for FR IIs, the entire volume occupied by the radio lobes is $V_\ell \simeq 1.6 \times 10^{69}$ cm. The radio core of 4C +67.13 coincides with the BCG, which is the brighter member of the galaxy pair CGPG 0719.8+6704, and which is offset by $\simeq 38'' \simeq 61$ kpc from the position of the cluster center (as inferred from the modeling of the cluster X-ray surface brightness distribution; see § 4.1.1 below).

The radio core of 4C +67.13 is distinguished by its inverted radio spectrum, with 1.5 GHz peak of 8.4 mJy beam^{-1} and 4.7 GHz peak of 12.1 mJy beam^{-1}. Subtracting the estimated contribution of the core flux from the lobes, the 1.5 GHz fluxes are 0.314 Jy (eastern) and 0.331 Jy (western), and the 4.7 GHz fluxes are 0.120 Jy (eastern) and 0.127 Jy (western). The resultant spectral indices for both lobes are 0.84 ± 0.12, assuming 10% uncertainties in each flux measurement, and the monochromatic lobes' radio power reads as $L_{1.5\,{\rm GHz}} \simeq 1.8 \times 10^{41}$ erg s^{-1}. The total fluxes and the lobe spectra from the VLA maps compare well with those derived
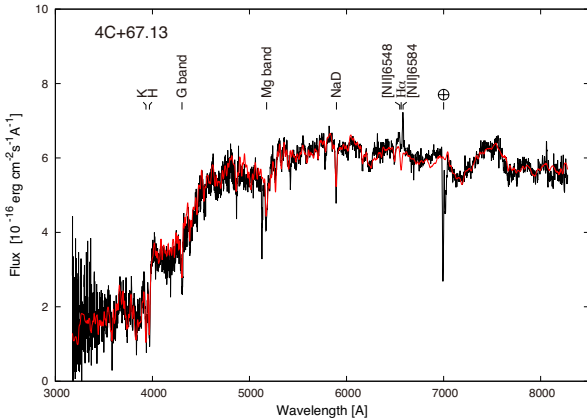
FIG. 2.— The rest frame optical spectrum of 4C +67.13, obtained with WHT. The observed spectrum is plotted in black while the STARLIGHT model is drawn in red. Unremoved telluric lines are marked with $\oplus$.

FIG. 3.— Observed [NII]λ6548,6584 + Hα blended emission lines of 4C +67.13 (plotted in black), with Gaussian profiles fitted to the emission lines overlaid in red. The reconstructed blend is drawn in blue in the top panel while the residuals are shown in the bottom panel.

detectable, and the resulting structure — characterized notably by sharp boundaries — appears highly symmetric in projection, we can not completely rule out this scenario.

3. OPTICAL SPECTROSCOPY

Optical spectroscopic observations of the BCG hosting 4C +67.13 and its neighboring galaxy were obtained with the WHT on 2010 April 21. Longslit spectra were taken using the Intermediate dispersion Spectrograph and Imaging System (ISIS) double-armed spectrograph with a chosen slit width of $1''$ (corresponding to 1.6 kpc). The slit was centered on the nucleus of 4C +67.13 and was oriented along the position angle of the galaxy pair ($PA = 93°$) so data were obtained for both objects. To identify and reject cosmic rays, the integration time was split into two 900 s exposures per arm. The average seeing FWHM during the observing run was about $0.8''$.

In the blue arm, the grism R300B was used and the detector was a thinned, blue-sensitive EEV12, array of 4096×2048 (13.5 micron) pixels with a spatial scale of $0.20''$ pixel^{-1}. The binning factor was 1×1 which yielded a wavelength coverage between about 3300 Å and 5300 Å with a dispersion of 0.86 Å pixel^{-1}. The instrumental resolution was 3 Å (FWHM) corresponding to $\sigma_{\mathrm{inst}} \sim 90$ km s^{-1}. In the red arm, the grism R158R with an order blocking filter GG495 was used. The detector was the default chip for the ISIS red arm, RED+, a red-sensitive array of 4096×2048 (15.0 micron) pixels with spatial scale $0.224''$ pixel^{-1}. The binning factor was 1×1 which yielded a wavelength coverage between about 5300 Å and 9000 Å with a dispersion of 1.82 Å pixel^{-1}. The instrumental resolution was 6 Å corresponding to $\sigma_{\mathrm{inst}} \sim 102$ km s^{-1}.

Reduction steps were performed for both spectral ranges separately using the NOAO IRAF packages. A master bias frame was created by averaging all the bias frames obtained during the observing night and subtracted from the science frames. Also, a master flat field frame was created and all 2D science frames were corrected for flat field, then cosmic rays were removed in combining the science exposures. Accurate wavelength calibration was performed using ArNe lamp exposures obtained before and after every target exposure and checked using sky lines, and the correction for optical distortion was applied. The contribution from the

from integrated measurements at 1.4 GHz (NVSS Condon et al. 1998) and 4.85 GHz (Gregory & Condon 1991) as well as the spectral index $\alpha = 0.88 \pm 0.08$ measured using 2.7, 5, and 10.7 GHz Effelsberg data (Reich et al. 2000). At lower frequencies, we derived $\alpha = 0.64 \pm 0.04$ by combining integrated fluxes at 74 MHz (Lane et al. 2012), 178 MHz (Gower et al. 1967), and 365 MHz (Douglas et al. 1996, assuming 15% uncertainty), together with the NVSS measurement, indicating flatter spectra below ~ 1 GHz.

The right panel in Figure 1 presents the VLA contours of the WAT radio galaxy located in the southern part of the Abell 578 cluster. The distance between the radio core of this source and the position of the cluster X-ray centroid is about $158''$, corresponding to 253 kpc.

Although 4C +67.13 lacks clearly defined hotspots, and its radio luminosity is intermediate between FR I and II sources according to the often considered luminosity divide, it should nonetheless be classified as an FR II radio galaxy. The original classification by Fanaroff & Riley (1974) is based on the ratio of the distance between the regions of the highest brightness on opposite sides of the radio core, to the total extent of the radio structure; sources with this ratio greater than 0.5 are classified as FR IIs ("edge-brightened radio morphology"). In the case of 4C +67.13, we obtain the ratio of $\simeq 0.65$ for the higher resolution map from Owen & Ledlow (1997), and 0.58 for the lower resolution map (Figure 1, left). The relatively low radio luminosity of the analyzed object compared with 'classical' FR IIs should not be considered as a surprise, as recent studies reveal the existence of a large number of FR IIs near and below the classical luminosity divide (Best 2009; Gendre et al. 2013). An alternative interpretation could be that the edge-brightened appearance of the radio lobes in 4C +67.13 is in fact only due to a special alignment of a 'narrow-angle tailed', i.e. intrinsically edge-dimmed radio structure viewed with its prolonged tails along our line of sight. That 4C +67.13 was selected for study from a parent sample (Owen & Ledlow 1997) where the BCGs predominantly show clear FR I morphology, would indicate an increase in the probability for such a special alignment. Although we think it is improbable that both tails would be aligned in such a way that their extended diffuse radio emission is un-
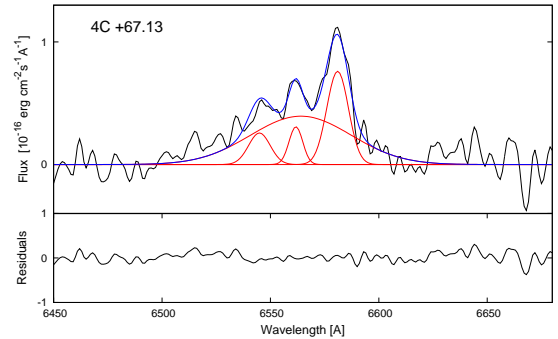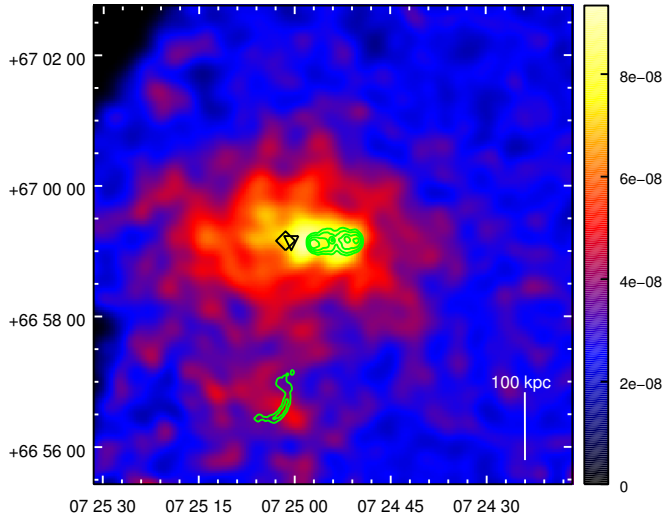
FIG. 4.— The exposure-corrected *Chandra* 0.5–7.0 keV image of Abell 578 with the VLA 4.7 GHz contours superimposed. X-ray point sources, including the nuclei of the two cluster radio galaxies, are removed from the image. The pixel size is equal to 4 times of the ACIS pixel size (i.e., $4 \times 0.492'' = 1.968''$) and the image is smoothed by a gaussian with $\sigma = 16\times$ the ACIS pixel size. Open black triangle and square denote the position of the cluster center obtained from the 2-dimensional fitting with elliptical and isotropic 2-D β models, respectively (see § 4.1.1.)

sky was determined from the sky regions at the two sides of the resulting spectrum, and then subtracted. The extraction of the 1D spectra was performed using APALL task. Scientific exposures were flux calibrated using the standard SP1257+038. The slit position angle falls along the radio jet/lobe axis, which is perpendicular to the optical photometric major axis so light from a region of $14.3'' \times 1''$ (23 kpc × 1.6 kpc) was summed into the 1D spectrum.

Before fitting the stellar continuum, the 1D spectra were corrected for Galactic extinction using the Schlegel et al. (1998) maps and the extinction law of Cardelli et al. (1989), shifted to the rest frame using a redshift of $z = 0.087227$ (Gomez et al. 1997) and resampled to $\Delta\lambda = 1$ Å. Analysis of the galaxy stellar continuum was performed using the STARLIGHT code (Cid Fernandes et al. 2005) which fits an observed spectrum with a linear combination of the simple stellar populations (SSPs) extracted from the models of Bruzual & Charlot (2003). Bad pixels and emission lines were masked and left out of the fits. Two bases of SSPs used in these fits: (1) $N_* = 150$ with 25 ages between 1 Myr and 18 Gyr and six metallicities from $Z = 0.005 \, Z_\odot$ to $2.5 \, Z_\odot$, and (2) $N_* = 45$ with 15 ages between 1 Myr and 13 Gyr and

TABLE 1
OPTICAL EMISSION LINES IN THE 4C +67.13 NUCLEUS

Line	Flux [10^{-15} erg cm^{-2} s^{-1}]	Position[a] [Å]	FWHM [km s^{-1}]
[NII]λ6548	0.30	6545.6	485.7
Hα$_{\rm narrow}$	0.32	6561.7	484.7
Hα$_{\rm broad}$	2.12	6567.9	2336.9
[NII]λ6584	0.895	6581.0	485.7

[a]The redshift of $z = 0.087227$ (Gomez et al. 1997) is adopted.

TABLE 2
RESULTS OF THE 2-DIMENSIONAL FITTING TO THE X-RAY IMAGE

Parameter	Value	
	Cluster region	
	isotropic	elliptical
Core radius r_C [kpc]	118^{+43}_{-29}	170^{+56}_{-38}
Center position α[a]	$7^{\rm h}25^{\rm m}01^{\rm s}.4^{+0.6}_{-0.6}$	$7^{\rm h}25^{\rm m}00^{\rm s}.6^{+0.6}_{-0.6}$
Center position δ[a]	$+66°59'10''^{+2}_{-3}$	$+66°59'09''^{+2}_{-2}$
Ellipticity ϵ	—	$0.32^{+0.04}_{-0.05}$
Ellipticity θ [degree]	—	$-3.2^{+4.3}_{-4.2}$
Amplitude[b] [10^{-9}]	$2.83^{+0.30}_{-0.25}$	$2.96^{+0.31}_{-0.26}$
Index β	$0.58^{+0.17}_{-0.10}$	$0.69^{+0.23}_{-0.12}$
reduced C-stat/dof	1.17/600	1.11/598
	Background region	
Constant[b] [10^{-9}]	$1.54^{+0.02}_{-0.02}$	
reduced C-stat/dof	1.15/1950	

[a]J2000 equinox
[b]photon pixel^{-2} cm^{-2} s^{-1}

three metallicities from 0.004 to $2.5 Z_\odot$. The results of the stellar populations and velocity dispersions obtained from the fits made with these two bases were consistent.

Stellar population fits to the observed spectrum of the BCG (Figure 2) revealed only old populations with 11 and 13 Gyr and metallicity of $0.02 Z_\odot$; no traces of young populations (with ages below a few Gyrs), indicative of a recently enhanced starformation, have been found in the modelling. The velocity dispersion obtained from the fits was $\sigma_\star = 321 \pm 17 \, {\rm km \, s^{-1}}$ which gives a SMBH mass of $\log M_{\rm BH}/M_\odot = 8.96 \pm 0.22$ based on the $M_{\rm BH} - \sigma_\star$ relation from Tremaine et al. (2002). Taking instead the $M_{\rm BH} - \sigma_\star$ relation from Ferrarese & Ford (2005), one obtains $\log M_{\rm BH}/M_\odot = 9.21 \pm 0.27$.

The [NII]λ6548,6584 and Hα lines in the stellar light subtracted spectra were fitted simultaneously with Gaussian profiles. Fitting was performed using the SPECFIT task in the STSDAS external IRAF package. Lines of the same ion were assumed to have the same offset and width and the additional constraint [NII]λ6584/[NII]λ6548 = 3 was further imposed on the line flux ratio. The results are presented in Figure 3 and Table 1 (where the provided line intensities are not extinction corrected). Detailed optical activity classification using line diagnostic diagrams (Kewley et al. 2006; Buttiglione et al. 2010) is not possible in the case of 4C +67.13 because only [NII] and Hα emission lines were detected with S/N ratio larger than 3. Nevertheless, these lines can still be used for a spectral diagnostic following Cid Fernandes et al. (2011), indicating that the 4C +67.13 nucleus is of a LINER type ('low-ionization nuclear emission-line region'). The Hα luminosity $L_{\rm H\alpha} = 5.9 \times 10^{39} \, {\rm erg \, s^{-1}}$ translates to the bolometric accretion-related luminosity $L_{\rm nuc} \simeq 10^{43} \, {\rm erg \, s^{-1}}$ (Sikora et al. 2013), or in the Eddington units $\Lambda \equiv L_{\rm nuc}/L_{\rm Edd} \simeq 10^{-4}$. This low accretion rate is confirmed by the analysis of the *Chandra* data for the 4C +67.13 nucleus presented below in § 4.2.2.

The analogous analysis performed for the second, fainter galaxy of the CGPG 0719.8+6704 pair revealed $\sigma_\star = 233 \pm 97 \, {\rm km \, s^{-1}}$, $\log M_{\rm BH}/M_\odot \simeq 8.3 - 8.7$, old stellar populations with a small addition of a younger one (1.43 Gyr, $Z = 0.05 Z_\odot$), and a LINER-type nucleus with
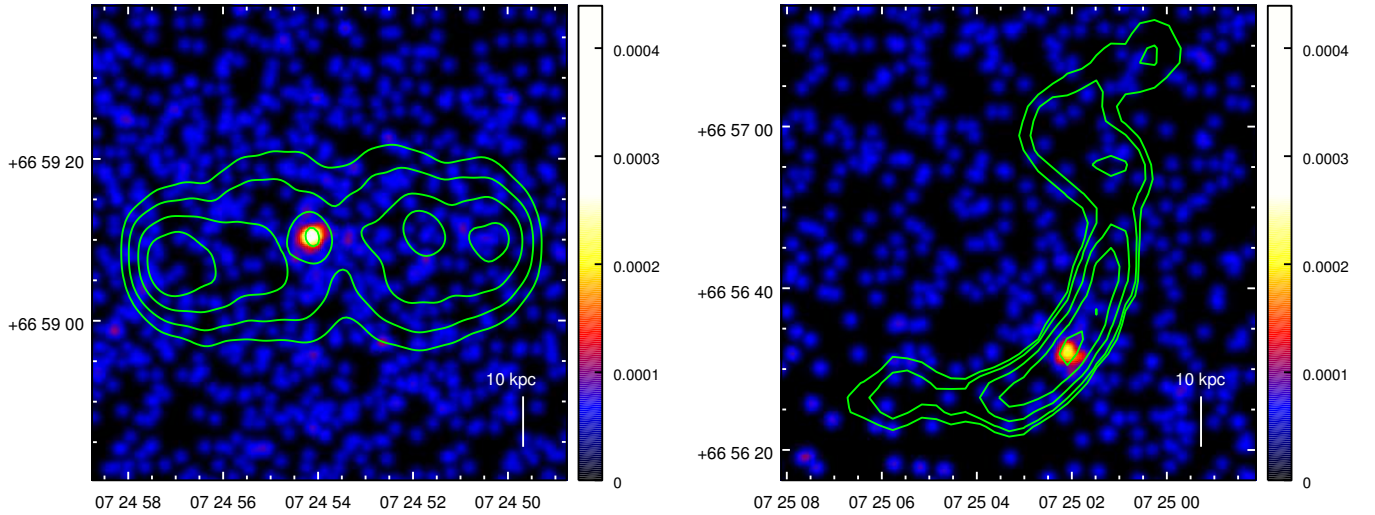
FIG. 5.— *Chandra* zoom-in images of the central part of the Abell 578 cluster around the position of 4C +67.13 (left), and of the southern part of the cluster around the position of the WAT radio galaxy (right), with the VLA 4.7 GHz radio contours superimposed. X-ray point sources are not removed from these figures. The pixel size is equal to a half of the ACIS pixel size (i.e., $0.5 \times 0.492''$). The image is smoothed by a Gaussian with $\sigma = $ ACIS pixel size.

$L_{H\alpha} \simeq 10^{40}\,\mathrm{erg\,s^{-1}}$ or $\Lambda \simeq 5 \times 10^{-4}$.

4. CHANDRA X-RAY OBSERVATIONS

Abell 578 was observed with *Chandra* on 2010 May 29 (obsid=11749) and July 23 (obsid=12225) using the ACIS-S detector. The source was placed on the back-illuminated CCD (S3) and the observations were made in very faint (VFAINT) mode with a total exposure time of 39.3 ks.

Analysis was performed with the CIAO version 4.5 software. We processed the data by running CIAO tool chandra_repro and applied the calibration files from CALDB 4.5.5.1. In order to obtain the highest angular resolution image, the sub-pixel algorithm EDSER was also applied. Event files of the two observations were merged into a single event file with reproject_obs for the image analysis. Point sources detected with wavdetect were removed, including also the nucleus of 4C +67.13, whose spectrum is analyzed separately in § 4.2.2. Besides the 4C +67.13 nuclear source, there were 15 X-ray sources found in the cluster region ($< 2.5'$ of the cluster center obtained in § 4.1.1) and 30 sources in the analyzed region. All events corresponding to the detected point sources are excluded from the analysis of the extended emission. Spectral extraction was performed with specextract and modeling was done in Sherpa (Freeman et al. 2001; Refsdal et al. 2009). The spectra and response files were extracted from the individual data and merged with combine_spectra. All spectral models were fitted to the data in the 0.5–7.0 keV energy range. Except for the radial profile analysis, we used the C-stat fitting statistics (Cash 1979) and the Nelder-Mead optimization method (Nelder & Mead 1965).

4.1. *Image Analysis*

Figure 4 shows the exposure-corrected and smoothed *Chandra* image of Abell 578 in the 0.5–7.0 keV energy band. Events of the two separate observations were summed to create the image. The green contours are from the VLA 4.7 GHz radio map discussed in § 2 above.

Figure 5 presents the *Chandra* zoom-in images of the central and southern parts of the cluster, around the positions of the two cluster radio galaxies (left and right panels, respectively). Point sources were not removed from these figures. No obvious small-scale X-ray sub-structures adjacent to the radio lobes can be noted, most likely due to the limited photon statistics.

4.1.1. *2-Dimensional Fitting*

To estimate the position of the cluster center and to extract the general characteristics of the cluster large-scale morphology, two-dimensional fits to the *Chandra* data was performed. Figure 6 shows the corresponding images of the background regions (upper panel) and of the cluster (middle and lower panels). Total counts are 11720 for the background and 8058 for the source.

First, we modeled the background image with the constant model (const2d) and the source image with the isotropic 2-D β model (beta2d). The regions around the two radio sources were removed from the analysis; these correspond to the circular black spots in the cluster images in Figure 6. In the fitting, an exposure map created by running flux_obs was used to correct non-uniformity of the effective area in the ACIS chip. The background model was fixed when fitting the source region. The fitting results are listed in Table 2. In particular, we found the position of the cluster center $(\alpha, \delta) = (7^{\mathrm{h}}25^{\mathrm{m}}01^{\mathrm{s}}.4^{+0.6}_{-0.6}, +66°59'10''^{+2}_{-3})$, the cluster core radius $r_C = 118^{+43}_{-29}$ kpc, and the index $\beta = 0.58^{+0.17}_{-0.10}$ (reduced fit C-statistic 1.17/600), consistent with the values obtained by Gomez et al. (1997).

We also modeled the source image with the elliptical 2-D β model. The results are given in the third column of Table 2. The thus evaluated position of the cluster center is consistent with the result of the isotropic β model, and the ellipticity parameters are $\epsilon = 0.32^{+0.04}_{-0.05}$ and $\theta = -3.2^{+4.3}_{-4.2}$ deg, while the other parameters changed only slightly ($r_C = 170^{+56}_{-38}$ kpc, $\beta = 0.69^{+0.23}_{-0.12}$). The elliptical model gives, however, a better fit with the reduced fit C-statistic of 1.11/598. In this way, we confirmed and robustly quantified the E-W elongation of
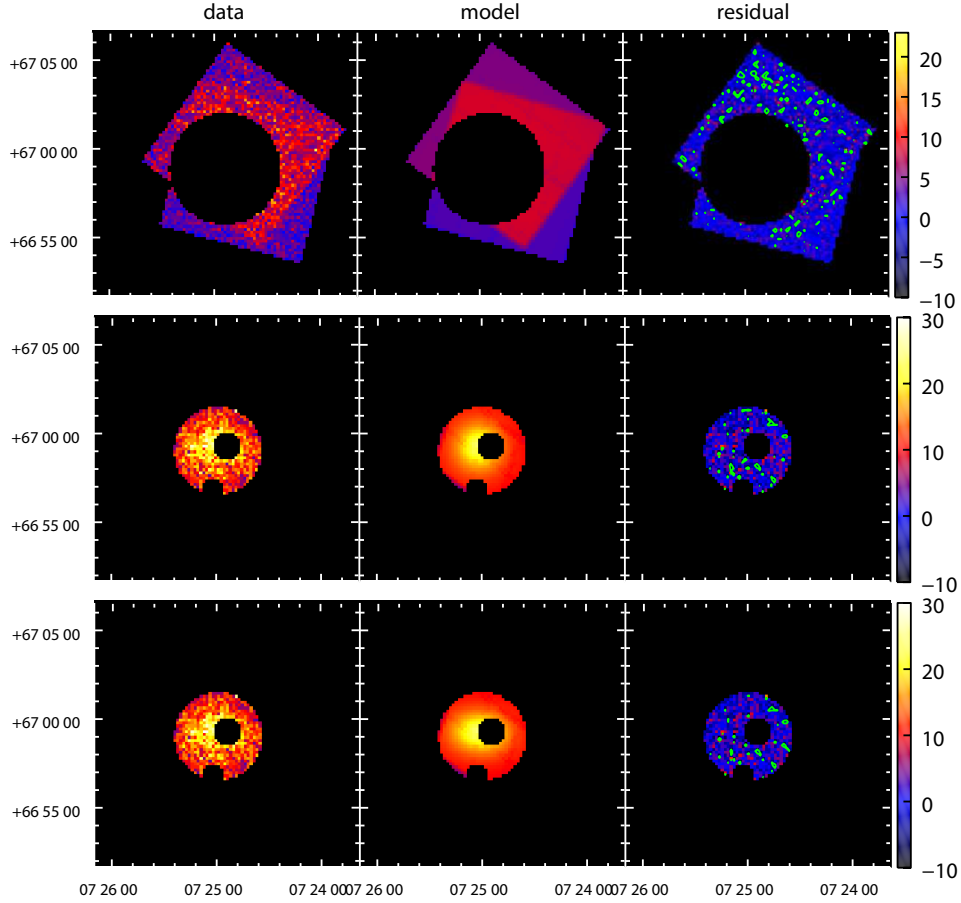
FIG. 6.— Two-dimensional analysis of the background (upper panel) and the Abell 578 cluster region (middle and lower panels). The ellipticity parameters are fixed to the circular symmetric values in the middle panel, while they are free parameters in the lower panel. The images of the data (left), adopted beta2d+const2d model (center), and residual (right) are shown in the same color scale. The green contours overlaid on the residual images represent ±2-sigma of the error of the data count in each pixel. The black regions in the images are ignored in the fitting. The pixel size is 9.84″ (20 times of the original ACIS pixel size).

the cluster mentioned by Gomez et al. (1997).

The positions of the cluster center obtained from our analysis are shown in Figure 4 where the black triangle and square denote the values obtained with the elliptical and isotropic models, respectively. The cluster center position is clearly offset from the position of the 4C +67.13 core. Our radio data indicate that the position of the 4C +67.13 core is $(7^h24^m54^s.150, +66°59'10.30'')$. Therefore, the offset in projection is $r_x \simeq 38''$, corresponding to 61 kpc for the elliptical cluster model.

4.1.2. *Radial Profiles*

A radial surface brightness profile of the central parts of the Abell 578 cluster was constructed from a pie region enclosed by the magenta solid line shown in Figure 7. The center of the pie region was set at the position of the cluster center obtained from the two-dimensional fitting discussed in the previous section. We extracted surface brightness from 20 annuli covering a radius of $150''$ ($\simeq 241$ kpc) by utilizing the dmextract tool. A pie region embedding within the 4C +67.13 radio source was ignored in order to exclude the expected contribution from the cluster gas interacting with the expanding radio lobes, as well as the X-ray emission of the radio galaxy itself (including the non-thermal emission of the extended lobes as well as the radiative output of the AGN and circumnuclear gas). We subtracted the surface bright-

ness of the region defined by a polygon as a background. Hereafter we refer to this background region as "background A." We fitted the background-subtracted surface flux profile with the beta1d model using the chi2datavar statistics. The fitting results are presented as the magenta curve in Figure 8, and the best-fit parameters are listed in Table 3.

In order to investigate the impact of the central radio source on the surrounding cluster gas and to further examine the cluster elongation, we also constructed radial surface brightness profiles separately for the north, east, south, and west parts of the cluster center. The respective black, red, green and blue dashed regions in Figure 7 were used to construct these profiles. Each region was divided into 8 annuli, with the radio lobes and X-ray point

TABLE 3
RESULTS OF THE X-RAY RADIAL PROFILE ANALYSIS

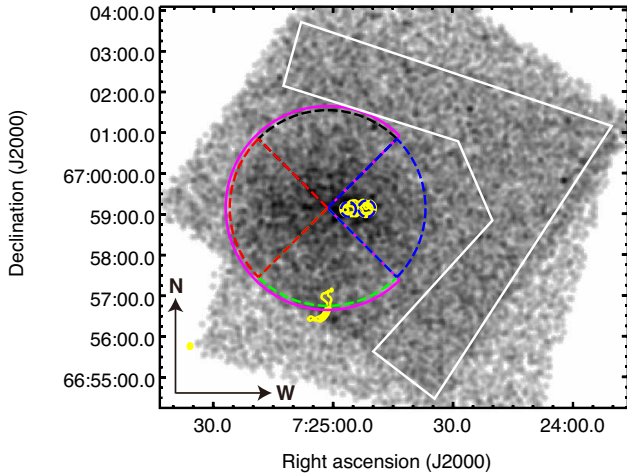| Parameter	Value
Core radius r_C [kpc]	138^{+49}_{-32}
Amplitude[a] $[10^{-9}]$	$2.80^{+0.23}_{-0.20}$
Index β	$0.71^{+0.26}_{-0.14}$
χ^2_ν/dof	1.25/17

[a] photon pixel^{-2} cm^{-2} s^{-1}

FIG. 7.— *Chandra* X-ray image of Abell 578 (gray scale) overlaid with the VLA 4.7 GHz contours (yellow). Different regions selected for constructing radial surface brightness profiles of the cluster are denoted by magenta, red, black, green, and blue contours (see § 4.1.2). Region defined by a white polygon was used to extract the background surface brightness ("background A").
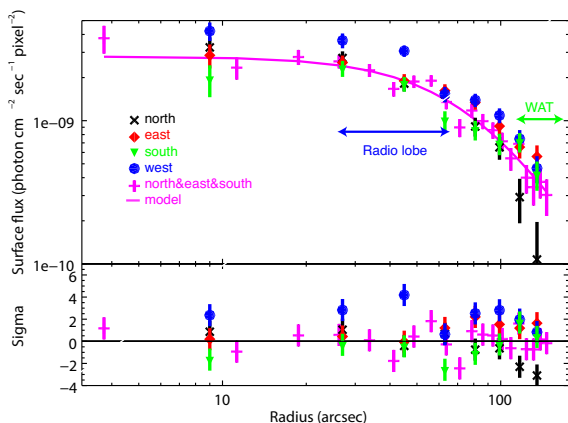

FIG. 8.— One-dimensional radial X-ray surface flux profiles of the Abell 578 cluster extracted from different regions defined in § 4.1.2 (color-coded symbols denote the corresponding regions in Figure 7). Thick magenta curve represents the best-fit beta1d+const1d model applied to the region enclosed by the magenta solid line in Figure 7.

sources removed. The profiles cover the regions from the center to a radius of $144''$ ($\simeq 231$ kpc) within an angle of $90°$. The results are shown in Figure 8. The cluster surface brightness in the western region (blue filled circles), where the central radio source 4C +67.13 is located, displays a clear excess over the average model. This may be due to the gas compression/heating by the expanding radio lobes. Also, for radii $\gtrsim 80''$, the surface brightness in the northern region (black crosses) is slightly lower than the average model, while that in the eastern region (red diamonds) slightly higher, consistent with the E-W elongation of the cluster atmosphere.

The last two data points in Figure 8 for the southern region (green triangles) overlap with the position of the

WAT radio galaxy. While we expect the elongation of the cluster to reduce the surface brightness along this direction compared to the average model, this effect is compensated for by the cluster substructure discussed also in Gomez et al. (1997), therefore no surface brightness decrement is seen.

4.2. *Spectral Analysis*
4.2.1. *Cluster Gas Around 4C +67.13*

The analysis presented in the previous section provided some indication for the interaction of the 4C +67.13 with the surrounding gas. In order to investigate in more detail the impact of the radio source on the cluster environment, we extracted spectra from four smaller pie regions around the cluster center, with the outer radius of $75''$, as shown in Figure 9. We refer to the western, eastern, northern, and southern regions as "source 1", "source 2", "source 3", and "source 4", respectively. From source 1, the emission from the positions of the radio lobes and the core of 4C +67.13 were once again removed. For the background, we chose the polygon region A, the same as the one used in constructing the cluster radial profiles (see § 4.1.2), and a large annular region "background B." While background A represents a uniform background in the ACIS chip — i.e., consisting of the Cosmic X-ray Background (CXB), Galactic Halo (GH) emission, and the instrumental background — background B was chosen to characterize the emission from the outer parts of the cluster adjacent to the selected source regions 1–4.

First we fitted the spectra of backgrounds A and B (total counts in the 0.5–7.0 keV energy band 3464 and 3487, respectively). For the instrument background, we used the model defined in "acis_bkg_model.py" [4] that consists of two power-laws and six gaussians. Parameters in the model were fixed at the values for ccd_id = 7, and only the normalization was a free parameter. We used a constant ARF by setting all values in specresp column to 100. The CXB and GH components were modeled by an absorbed power-law model and an unabsorbed thermal plasma model APEC, respectively. The photon index of the CXB was fixed at 1.41 (De Luca & Molendi 2004) and the temperature of the GH was fixed at 0.2 keV (Kuntz & Snowden 2000). The absorption column density for the CXB was fixed at the Galactic value, 4.39×10^{20} cm^{-2}. The spectrum of background B was modeled by the background A scaled for the extraction region and an APEC model with Galactic absorption. The redshift of the APEC model for background B was fixed at 0.0866, and the abundance was allowed to vary. The obtained best-fit parameters of backgrounds A and B are listed in Table 4. The resulting normalization of the CXB component 12.4 ± 1.5 ph keV^{-1} cm^{-2} s^{-1} str^{-1} at 1 keV is consistent with that of De Luca & Molendi (2004). These background model parameters were then fixed in the following analysis.

In the above, we have assumed that background A does not contain any significant cluster emission. We verified this assumption by adding an APEC component with Galactic absorption to the model for background A and obtained an upper limit for the APEC normalization,

---

[4] https://github.com/taldcroft/datastack/blob/master/acis_bkg_model.py
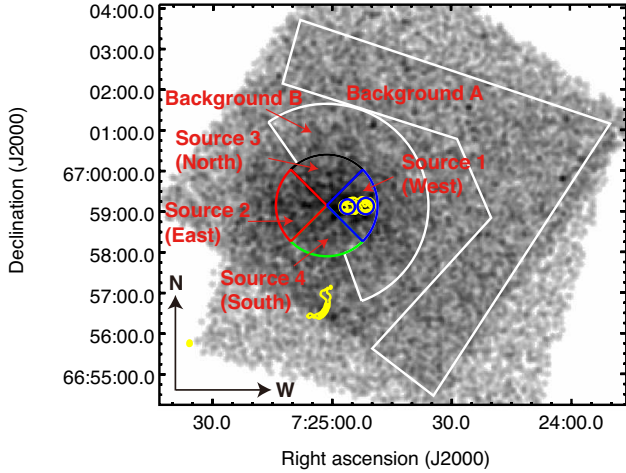
FIG. 9.— *Chandra* X-ray image of Abell 578 (gray scale) overlaid with the VLA 4.7 GHz contours (yellow). Different regions selected for the cluster spectral analysis are denoted by red, black, green, and blue contours (see § 4.2.1). Regions defined by white polygons were used to extract the background spectra ("background A" and "background B").

Model component	Parameter	Value
background A		
Instrumental background	normalization	$31.42^{+0.73}_{-0.72}$
Cosmic X-ray background	photon index	1.41 (fix)
	norm[a] $[10^{-6}]$	$23.7^{+2.9}_{-2.8}$
Galactic Halo	kT [keV]	0.2 (fix)
	norm[b] $[10^{-6}]$	$5.3^{+3.2}_{-3.1}$
Fit statistics	reduced C-stat/dof	0.64/60
background B		
Cluster gas emission	Abundance	$0.34^{+0.23}_{-0.15}$
	kT [keV]	$2.50^{+0.43}_{-0.37}$
	norm[b] $[10^{-3}]$	$0.56^{+0.07}_{-0.07}$
	density $[10^{-3} \text{ cm}^{-3}]$	$0.78^{+0.05}_{-0.05}$
Fit statistics	reduced C-stat/dof	1.04/51

[a] Normalization of the power-law model in units of photon cm^{-2} s^{-1} at 1 keV.
[b] Normalization of the APEC model defined as $10^{-14}/(4\pi [D_A(1+z)]^2) \int n_e n_H dV$.

with the 90% confidence intervals of 7.6×10^{-6} for 2 keV and 2.4×10^{-6} for 1 keV, where the temperature of the APEC component is fixed. Since the backscale value of source 1 is ~ 0.1, this upper limit corresponds therefore to a negligible amount of the APEC component for source 1 spectrum.

Next we used the CIAO Sherpa extension package de-project[5] (Siemiginowska et al. 2010) for spectral analysis of the selected source regions. Here, we assumed spherical symmetry for the cluster gas. In the analysis, the spectral model was composed of a linear weighted combination of a source model, the background B model, and the background A model was scaled by the backscale value: rsp(W_{src}*src_model+W_{bkg}*bkgB_model) + bkg_scale*(bkgA_rsp(bkgA_model)). The weight was defined as a volume of extraction region normalized by a volume of a sphere enclosing background B. The weight was calculated in the deproject tool except for the source 1, for which the weight was calculated by Monte-Carlo integration. The weight of the source 1 region is 0.0245852 ± 0.0000008 and that of background B for the source 1 analysis is 0.0462102 ± 0.0000009. We assumed an APEC model with Galactic absorption for each spectrum. We fixed the abundance at 0.0, 0.5 and 1.0 at first, and then set it free.

X-ray spectra and spectral fits for the source 1 and the combined source 2+3+4 regions are shown in Figure 10; the model parameters for the abundance $A = 0.5$ are listed in Table 5. The total counts in the 0.5–7.0 keV energy band were 838 for source 1, 884 for source 2, 880 for source 3, 773 for source 4, and 2537 for source 2+3+4. The corresponding contour plots of temperature versus normalization are shown in Figure 11. For all the considered abundance values, source 1 (blue) is located at the upper right in the contour plots, which implies that the cluster gas around 4C +67.13 is indeed denser and hotter

than that in the other selected regions, consistent with shock heating due to the expanding radio lobes. The reduced C-stat of the spectral fit for source 1 were 1.44, 1.33, 1.36 and 1.37 for the abundance 0, 0.5, 1 and free, respectively. Also, for the combined source 2+3+4, the reduced C-stat is best at the abundance of 0.5; hereafter we adopt the fitting results with the abundance fixed at this value. The temperature ratio of source 1 to the combined source 2+3+4 is then $1.37^{+0.30}_{-0.18}$, and the density ratio is $1.36^{+0.06}_{-0.06}$. These values correspond to shock Mach numbers of $\mathcal{M}_{sh} \simeq 1.38$ and 1.24, respectively.

4.2.2. 4C +67.13 Nucleus

Finally, we analyzed the X-ray spectrum of the active nucleus in 4C +67.13. The spectrum was extracted from a circular region with 1.5″ radius while the background spectrum was extracted from the annular region from 3″ to 11″. The total number of counts in the 0.5–7.0 keV energy band is 59 for the source region and 88 for the background region.

The background spectrum was fitted by the model used in the fitting of background A plus an APEC model moderated by the Galactic absorption. The normalizations of the instrumental background, as well as of the CXB and GH, were fixed at the values obtained in section 4.2.1, and scaled by the areas of the extraction regions. Abundance was fixed at 1.0, and the redshift was fixed at 0.0866. The best-fit model parameters obtained are listed in Table 6. Note that the emerging temperature of 3.0 keV is consistent with that obtained in spectral fitting of the source 1 region in § 4.2.1.

In the first attempt, the source (4C +67.13 nucleus) spectrum was fitted by a cosmologically redshifted power-law model with the Galactic absorption. The background model was fixed and the obtained best-fit parameters are listed in Table 6. In this case, the photon index of the power-law model obtained is quite large ($\Gamma = 2.8$), and this model does not provide a very good fit (C-stat $= 12.4/10$) due to a prominent excess around 1 keV in the data. We have therefore added an additional thermal component to the fitted source spectrum
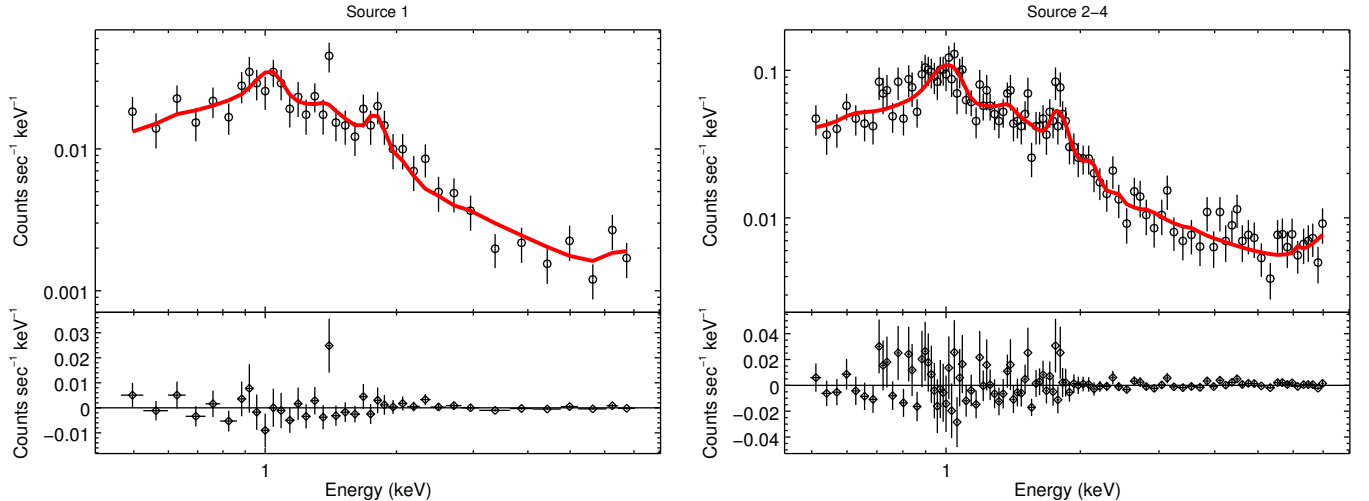
Fig. 10.— Top panels show the observed X-ray spectra and spectral fits (with the abundance fixed at 0.5; red line) for the source 1 (left) and the source 2+3+4 (right) regions (see § 4.2.1). Bottom panels show the differences between the observed data and the model.

TABLE 5
Best-fit model X-ray parameters for the sources 1–4

Parameter	Value				
	source 1	source 2	source 3	source 4	source 2+3+4
	West	East	North	South	North & East & South
Abundance	0.5 (fix)	0.5 (fix)	0.5 (fix)	0.5 (fix)	0.5 (fix)
kT [keV]	$2.73^{+0.57}_{-0.31}$	$2.04^{+0.26}_{-0.22}$	$1.95^{+0.21}_{-0.26}$	$1.98^{+1.23}_{-0.46}$	$2.00^{+0.13}_{-0.14}$
norm[a] $[10^{-3}]$	$2.67^{+0.19}_{-0.18}$	$1.69^{+0.17}_{-0.16}$	$1.62^{+0.17}_{-0.16}$	$1.07^{+0.18}_{-0.24}$	$1.46^{+0.09}_{-0.09}$
density $[10^{-3}\,\mathrm{cm}^{-3}]$	$1.71^{+0.06}_{-0.06}$	$1.36^{+0.07}_{-0.07}$	$1.33^{+0.07}_{-0.07}$	$1.08^{+0.09}_{-0.12}$	$1.26^{+0.04}_{-0.04}$
reduced C-stat/dof	1.33/37	1.15/38	0.79/39	0.99/34	1.19/100

[a]normalization of APEC model

(consistently with the analysis results for LINER sources in general; see Younes et al. 2011), obtaining this time an acceptable fit with C-stat $= 4.2/8$ (see Table 6) and a more reasonable photon index of $\Gamma = 2.1$. The resulting temperature of the additional thermal component is $0.96\,\mathrm{keV}$ and the normalization of the power-law component is $1.8 \times 10^{-6}\,\mathrm{photon\,keV^{-1}\,cm^{-2}\,s^{-1}}$. The total nuclear 2–10 keV flux in the source rest frame is $F_{2-10\,\mathrm{keV}} \simeq 3.4 \times 10^{-15}\,\mathrm{erg\,cm^{-2}\,s^{-1}}$, corresponding to the isotropic luminosity of $L_{2-10\,\mathrm{keV}} \simeq 6.2 \times 10^{40}\,\mathrm{erg\,s^{-1}}$. This is consistent with the bolometric accretion-related luminosity L_{nuc} estimated in § 3 above, assuming the bolometric correction factor of the order of $L_{\mathrm{nuc}}/L_{2-10\,\mathrm{keV}} \sim 100$, as in fact expected (Vasudevan & Fabian 2007; Ho 2008).

5. DISCUSSION AND CONCLUSIONS

The Abell 578 system provides an interesting insight into the widely debated cluster formation processes. Velocity measurements for the member galaxies presented by Gomez et al. (1997) indicated that this system is not relaxed, and consists of the two interacting sub-clusters. Our analysis of newly obtained *Chandra* data allowed us to confirm their results based on ROSAT PSPC data for the dominant sub-cluster and to quantify them robustly. In particular, we found the ellipticity parameter for the cluster X-ray atmosphere $\epsilon \simeq 0.3$ (i.e., elongated east-west), and an offset of about $r_x \simeq 60\,\mathrm{kpc}$ between the BCG which hosts the 4C +67.13 radio galaxy and

the centroid of the cluster X-ray emission (inferred from the two-dimensional fitting of the surface brightness distribution of the diffuse emission component). Similar displacements have been found in a substantial number of galaxy clusters (e.g., Patel et al. 2006; Haarsma et al. 2010; Hashimoto et al. 2014). Recently, Lauer et al. (2014) demonstrated that the distribution of the projected spatial offsets is a steep power-law function of cluster radius with a median value of about 10 kpc. The displacement we found for Abell 578/4C +67.13 is therefore larger than in most clusters although not as extreme as in some other cases (such as, e.g., Coma cluster with $r_x \simeq 260\,\mathrm{kpc}$), and is also smaller than the Abell 578 cluster core radius $r_C \simeq 170\,\mathrm{kpc}$ (evaluated here for the assumed β-profile with best-fit index $\beta \simeq 0.7$).

The position of the BCG with respect to the X-ray centroid of the cluster is considered a measure of the evolutionary state of a system. In particular, these offsets imply deviations from the dynamical equilibrium at earlier stages of a cluster formation via hierarchical merging (see, e.g., Martel et al. 2014). In addition, the presence of the offsets generally supports the idea that BCGs are formed via galaxy mergers in one of the infalling groups prior to the cluster assembly (see the discussion in, e.g., Merritt 1985; Dubinski 1998; Katayama et al. 2003). In this context, we note that the BCG studied here is a member of the galaxy pair CGPG 0719.8+6704 (*R*-band
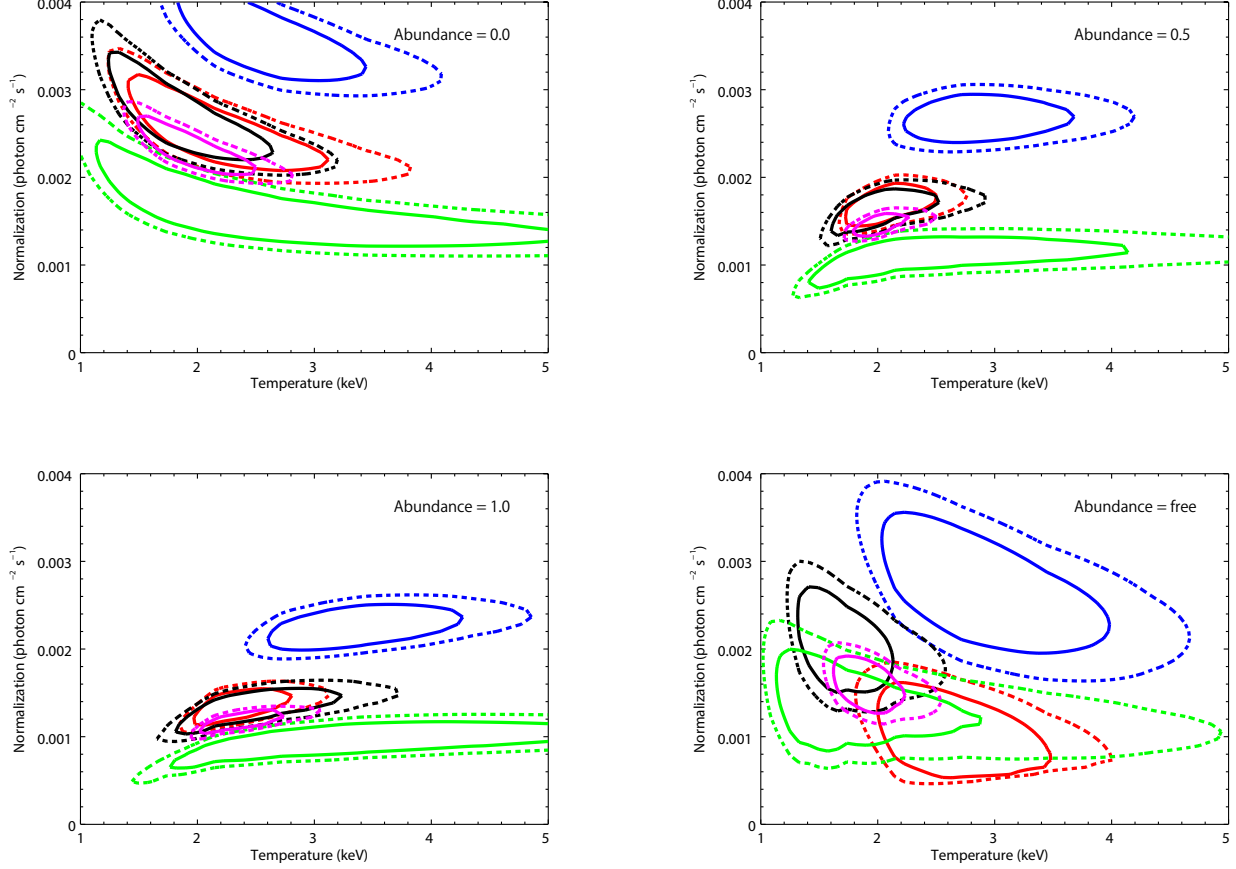
FIG. 11.— Contour plots of temperature versus normalization corresponding to the spectral fits with different abundance values: 0.0 (top left), 0.5 (top right), 1.0 (bottom left) and free (bottom right). In each panel, the solid and dashed curves denote the 68% and 90% confidence levels, respectively, for the northern (black), eastern (red), southern (green), and western (blue) parts of the Abell 578 cluster as discussed in § 4.2.1 as shown in Figure 9 with the same color-coding. The contours for the combined east+north+south region are indicated in magenta.

magnitudes of 13.6 and 14.8), with the projected separation of about 10 kpc, and with no or only little young stellar populations. The performed optical spectroscopy allowed us also to estimate the black hole masses (from the observed velocity dispersion) for the two members of the pair as $M_{BH} \sim 10^9 M_\odot$ and $3 \times 10^8 M_\odot$, respectively. The analysis of the emission lines indicated moreover that both galactic nuclei are active, albeit at a low level (LINER-type AGN), with the corresponding nuclear luminosities of $L_{nuc} \sim 10^{43}$ erg s^{-1}. However, only the brighter member of the pair is radio-loud.

The accretion rate for the 4C +67.13 host is relatively low, namely $\dot{M}_{acc} = L_{nuc}/\eta_d c^2 \sim 0.01 M_\odot$ yr^{-1} ~ $5 \times 10^{-4} \dot{M}_{Edd}$, assuming the radiative efficiency of the accretion disk $\eta_d \simeq 0.02$ (following Sharma et al. 2007). This is comparable to the accretion rate derived by Stawarz et al. (2014) for the analogous radio galaxy PKS B1358−113 located at the center of the Abell 1836 cluster. Despite such a limited accretion rate, both AGN are able to launch luminous jets surrounded by FR II-type radio lobes. Interestingly, the *maximum* jet kinetic power in the source studied here, for the given accretion rate as estimated above, reads as $L_{j/(max)} \simeq 3 \dot{M}_{acc} c^2 \sim 2 \times 10^{45}$ erg s^{-1} (see McKinney et al. 2012), which indeed

is in the range of the jet kinetic luminosities typically derived for "classical" FR IIs (e.g., Machalski et al. 2007).

We note, on the other hand, that it is quite plausible that the nuclear accretion rate in 4C +67.13 has dropped significantly since the onset of the jet activity in the source, i.e. during the last $\sim 1 - 10$ Myr. And in fact, the lack of prominent hotspots at the edges of the radio lobes could be considered as an indication for a recently quenched/suppressed jet production in the system (due to a sudden decrease in the accretion rate), since jet termination shocks in FR II-type radio galaxies are expected to die out almost immediately (i.e., on the timescales of $\sim 10^4 - 10^5$ yr) after the supply of the jet momentum ceases (see in this context the discussion in Carilli & Barthel 1996, and references therein). If correct, this could suggest in general a highly modulated jet duty cycle of BCGs, consisting of short but intense ("FR II-like") episodes of the enhanced jet activity, separated by the extended ("FR I-like") periods of a quiescence/low-level activity.

In this context, we note that the existing scaling relations between the jet kinetic power and the lobes' radio luminosity for radio galaxies located at the centers of galaxy clusters have been derived assuming a relatively

TABLE 6
Best-fit model parameters for the 4C +67.13 nucleus

Parameter	Value	
Source region		
Model	power-law	power-law+apec
photon index	$2.8^{+0.3}_{-0.3}$	$2.1^{+0.5}_{-0.4}$
norm[a] $[10^{-6}]$	$4.5^{+0.6}_{-0.6}$	$1.8^{+1.1}_{-1.0}$
kT [keV]	—	$0.96^{+0.15}_{-0.12}$
norm[b] $[10^{-6}]$	—	$2.0^{+0.8}_{-0.8}$
reduced C-stat/dof	1.24/10	0.52/8
Background region		
Abundance	1.0 (fix)	
kT [keV]	$3.01^{+2.02}_{-0.94}$	
norm[b] $[10^{-6}]$	$51.3^{+9.6}_{-9.4}$	
reduced C-stat/dof	1.26/6	

[a]Normalization of the power-law model in units of photons keV^{-1} cm^{-2} s^{-1} at 1 keV in the source rest frame.
[b]Normalization of the APEC model.

slow (sonic) expansion of the jet cocoons in a pressure equilibrium with the surrounding cluster gas (Bîrzan et al. 2008; Cavagnolo et al. 2010; O'Sullivan et al. 2011). When applied to 4C +67.13, these relations give in particular $L_{j/(\mathrm{rad})} \sim (2-7) \times 10^{44}$ erg s^{-1}. The main assumption involved here may however be justified only in the case of FR I systems, but not FR II-type radio sources which likely expand with supersonic velocities; with such a rapid expansion, leading to the formation of bow-shocks in the surrounding intracluster medium, the jet kinetic power should be therefore larger than the corresponding value of $L_{j/(\mathrm{rad})}$.

Our *Chandra* data do not provide any *direct* evidence for the presence of a shock driven in the center of Abell 578 by a supersonic expansion of the 4C +67.13 lobes, but this may only be due to the limited photon statistics. Instead, our detailed analysis of the available X-ray maps did reveal that the cluster gas in the vicinity of 4C +67.13 seems to be compressed by a factor of about 1.4 (i.e., the gas number density increased by this factor) and heated (from $kT \simeq 2.0$ keV up to 2.7 keV), consistent with a weak, $\mathcal{M}_{sh} \sim 1.3$ shock driven by the expanding jet cocoon. Analogous weak shocks have been found in much deeper *Chandra* and XMM-*Newton* exposures of several rich clusters (e.g., Nulsen et al. 2005; Fabian et al. 2006; Wilson et al. 2006; Gitti et al. 2007; Wise et al. 2007; Simionescu et al. 2007; Reynolds et al. 2008; Lal et al. 2010; Blanton et al. 2011; Cavagnolo et al. 2011; Croston et al. 2011), and further, often tentative detections have been reported for a number of other

(poorer) systems, including PKS B1358−113 (Stawarz et al. 2014, and references therein).

One should keep in mind, at the same time, that the aforementioned limited photon statistics following from a rather short *Chandra* exposure of a relatively low-luminosity system, precludes us from making definite statements on the precise gas density and temperature structure in the central parts of Abell 578. In particular, it is plausible that the elongated X-ray core of the cluster, together with the large offset between the position of the BCG and the X-ray centroid inferred from the modeling of the diffuse emission component, are related instead to the sloshing of the intracluster medium triggered by the ongoing merger processes (e.g., Tittley & Henriksen 2005; ZuHone et al. 2010). Only very deep follow-up observations of the studied system can resolve this issue by revealing directly the surface brightness and temperature discontinuities consistent with "cold fronts" — expected in the case of a gas sloshing — rather than weak shocks (see in this context Markevitch & Vikhlinin 2007).

Altogether, the multifrequency data gathered here for the Abell 578 cluster reveal an insightful snap-shot of a complex system in formation. At its present stage, it appears that the cluster galaxies and intracluster gas are falling onto the center of the cluster potential, evolving slowly toward a dynamical equilibrium, while the cluster atmosphere is heated gently by the radio jets/lobes produced with high efficiency in the low-accretion rate nucleus of the brightest cluster galaxy. The overall cluster luminosity $L_{0.5-7.0\,\mathrm{keV}} \simeq 2 \times 10^{43}$ erg s^{-1} and temperature $kT \gtrsim 2$ keV are on the other hand unexceptional, being consistent with the X-ray luminosity-temperature correlation established for clusters and groups of galaxies (see, e.g., Sun 2012).

REFERENCES

Antognini, J., Bird, J., & Martini, P. 2012, ApJ, 756, 116
Belsole, E., Worrall, D. M., Hardcastle, M. J., & Croston, J. H. 2007, MNRAS, 381, 1109
Best, P. N. 2009, Astronomische Nachrichten, 330, 184
Bîrzan, L., McNamara, B. R., Nulsen, P. E. J., Carilli, C. L., & Wise, M. W. 2008, ApJ, 686, 859
Blanton, E. L., Randall, S. W., Clarke, T. E., et al. 2011, ApJ, 737, 99
Bruzual G., & Charlot S. 2003, MNRAS, 344, 1000
Buttiglione, S., Capetti, A., Celotti, A., et al. 2010, A&A, 509, A6
Cardelli J. A., Clayton G. C., Mathis J. S. 1989, ApJ, 345, 245
Carilli, C. L., & Barthel, P. D. 1996, A&ARv, 7, 1
Cash, W. 1979, ApJ, 228, 939

Cavagnolo, K. W., McNamara, B. R., Nulsen, P. E. J., et al. 2010, ApJ, 720, 1066
Cavagnolo, K. W., McNamara, B. R., Wise, M. W., et al. 2011, ApJ, 732, 71
Cid Fernandes, R., Mateus, A., Sodré, L., Stasińska, G., & Gomes, J. M. 2005, MNRAS, 358, 363
Cid Fernandes, R., Stasińska, G., Mateus, A., & Vale Asari, N. 2011, MNRAS, 413, 1687
Condon, J. J., Cotton, W. D., Greisen, E. W., et al. 1998, AJ, 115, 1693
Crawford, C. S., Allen, S. W., Ebeling, H., Edge, A. C., & Fabian, A. C. 1999, MNRAS, 306, 857

12

Croston, J. H., Hardcastle, M. J., Mingo, B., et al. 2011, ApJ, 734, L28

De Luca, A., & Molendi, S. 2004, A&A, 419, 837

Douglas, J. N., Bash, F. N., Bozyan, F. A., Torrence, G. W., & Wolfe, C. 1996, AJ, 111, 1945

Dubinski, J. 1998, ApJ, 502, 141

Fabian, A. C. 2012, ARA&A, 50, 455

Fabian, A. C., Sanders, J. S., Taylor, G. B., et al. 2006, MNRAS, 366, 417

Fanaroff, B. L. and Riley, J. M. 1974, MNRAS, 167, 31P

Ferrarese, L., & Ford, H. 2005, SSRv, 116, 523

Freeman, P., Doe, S., Siemiginowska, A. 2001, Proc. SPIE, 4477, 76

Gendre, M. A., Best, P. N., Wall, J. V., & Ker, L. M. 2013, MNRAS, 430, 3086

Gitti, M., McNamara, B. R., Nulsen, P. E. J., & Wise, M. W. 2007, ApJ, 660, 1118

Gomez, P. L., Ledlow, M. J., Burns, J. O., Pinkey, J., & Hill, J. M. 1997, AJ, 114, 1711

Gower, J. F. R., Scott, P. F., & Wills, D. 1967, MmRAS, 71, 49

Gregory, P. C., & Condon, J. J. 1991, ApJS, 75, 1011

Haarsma, D. B., Leisman, L., Donahue, M., et al. 2010, ApJ, 713, 1037

Hashimoto, Y., Henry, J. P., & Boehringer, H. 2014, MNRAS, 440, 588

Ho, L. C. 2008, ARA&A, 46, 475

Katayama, H., Hayashida, K., Takahara, F., & Fujita, Y. 2003, ApJ, 585, 687

Kewley, L. J., Groves, B., Kauffmann, G., & Heckman, T. 2006, MNRAS, 372, 961

Kormendy, J., & Ho, L. C. 2013, ARA&A, 51, 511

Kuntz, K. D. & Snowden, S. L. 2000, MNRAS, 543, 195

Lal, D. V., Kraft, R. P., Forman, W. R., et al. 2010, ApJ, 722, 1735

Lane, W. M., Cotton, W. D., Helmboldt, J. F., & Kassim, N. E. 2012, Radio Science, 47, RS0K04

Lauer, T. R., Postman, M., Strauss, M. A., Graves, G. J., & Chisari, N. E. 2014, ApJ, 797, 82

Machalski, J., Chyży, K. T., Stawarz, Ł., & Kozieł, D. 2007, A&A, 462, 43

Markevitch, M., & Vikhlinin, A. 2007, Phys. Rep., 443, 1

Martel, H., Robichaud, F., & Barai, P. 2014, ApJ, 786, 79

Mathews, W. G., & Guo, F. 2011, ApJ, 738, 155

McKinney, J. C., Tchekhovskoy, A., & Blandford, R. D. 2012, MNRAS, 423, 3083

McNamara, B. R., & Nulsen, P. E. J. 2012, New Journal of Physics, 14, 055023

Merritt, D. 1985, ApJ, 289, 18

Nelder, J. A., & Mead, R. 1965, Comput. J., 7, 308

Nulsen, P. E. J., Hambrick, D. C., McNamara, B. R., et al. 2005, ApJ, 625, L9

O'Dea, C. P. 1998, PASP, 110, 493

O'Sullivan, E., Giacintucci, S., David, L. P., et al. 2011, ApJ, 735, 11

Owen, F. N., & Ledlow, M. J. 1997, ApJS, 108, 41

Owen, F. N., White, R. A., & Burns, J. O. 1992, ApJS, 80, 501

Owen, F. N. Ledlow, M. J., & Keel, W. C. 1995, ApJ, 109, 14

Patel, P., Maddox, S., Pearce, F. R., Aragón-Salamanca, A., & Conway, E. 2006, MNRAS, 370, 851

Refsdal, B. L., Doe, S. M., Nguyen, D. T., et al. 2009, in Proc. 8th Python in Science Conference, eds. G. Varoquaux, S. van der Walt, & J. Millman, 51

Reich, W., Fürst, E., Reich, P., et al. 2000, A&A, 363, 141

Reynolds, C. S., Casper, E. A., & Heinz, S. 2008, ApJ, 679, 1181

Siemiginowska, A., Burke, D. J., Aldcroft, T. L., et al. 2010, ApJ, 722, 102

Schlegel D. J., Finkbeiner D. P., Davis M. 1998, ApJ, 500, 525

Sharma, P., Quataert, E., Hammett, G. W., & Stone, J. M. 2007, ApJ, 667, 714

Shepherd, M. C., Pearson, T. J., & Taylor, G. B. 1994, BAAS, 26, 987

Siemiginowska, A., Cheung, C. C., LaMassa, S., et al. 2005, ApJ, 632, 110

Sikora, M., Stasińska, G., Kozieł-Wierzbowska, D., Madejski, G. M., & Asari, N. V. 2013, ApJ, 765, 62

Simionescu, A., Böhringer, H., Brüggen, M., & Finoguenov, A. 2007, A&A, 465, 749

Stawarz, L., Szostek, A., Cheung, C. C., et al. 2014, ApJ, 794, 164

Sun, M. 2012, New Journal of Physics, 14, 045004

Tittley, E. R., & Henriksen, M. 2005, ApJ, 618, 227

Tremaine, S., Gebhardt, K., Bender, R., et al. 2002, ApJ, 574, 740

Vasudevan, R. V. & Fabian, A. C. 2007, MNRAS, 381, 1235

Voit, G. M., & Donahue, M. 2005, ApJ, 634, 955

Wilson, A. S., Smith, D. A., & Young, A. J. 2006, ApJ, 644, L9

Wing, J. D., & Blanton, E. L. 2011, AJ, 141, 88

Wise, M. W., McNamara, B. R., Nulsen, P. E. J., Houck, J. C., & David, L. P. 2007, ApJ, 659, 1153

York, D. G., Adelman, J., Anderson, J. E., Jr., et al. 2000, AJ, 120, 1579

Younes, G., Porquet, D., Sabra, B., & Reeves, J. N. 2011, A&A, 530, A149

Zirbel, E. L. 1997, ApJ, 476, 489

ZuHone, J. A., Markevitch, M., & Johnson, R. E. 2010, ApJ, 717, 908

Zwicky, F. 1971, Catalogue of Selected Compact Galaxies and of Post-Eruptive Galaxies, Guemligen, Switzerland